3D-multilayer simulation of microstructure and mechanical properties of porous materials by selective sintering

Xiandong Zhou[1] | Yangyiwei Yang[1] | Somnath Bharech[1] | Binbin Lin[1] | Jörg Schröder[2] | Bai-Xiang Xu[1]

[1]Mechanics of Functional Materials Division, Technische Universität Darmstadt, Darmstadt, Hessen, Germany

[2]Abteilung Bauwissenschaften, Fakultät für Ingenieurwissenschaften, Institut für Mechanik, Universität Duisburg-Essen, Essen, Germany

Correspondence
Yangyiwei Yang and Bai-Xiang Xu, Mechanics of Functional Materials Division, Technische Universität Darmstadt, Darmstadt, Hessen, Germany.
Email:
yangyiwei.yang@mfm.tu-darmstadt.de
and xu@mfm.tu-darmstadt.de

Abstract

This work presents multilayer phase-field simulation of selective sintering process and the calculation of effective mechanical properties and residual stress of the microstructure using the finite element method. The dependence of the effective properties and residual stress on the process parameters, such as beam power and scan speed, are analyzed. Significant partial melting of powders is observed for large beam power and low scan speed, which results in low porosity of the microstructure. Nonlinear relationship between the effective mechanical properties and process parameters is observed. The increasing rate of effective mechanical properties decreases with increasing beam power, while increases with decreasing scan speed. The dependence of effective Young's modulus and Poisson's ratio on porosity are well established using power law models. Stress concentrations are found at the necking region of powders and the intensity increases with the level of partial melting, which results in increasing residual stress in the microstructure. The numerical results reveal quantitatively the process-microstructure-property relation, which implies the feasibility of the subsequent data-driven approach.

KEYWORDS

additive manufacturing, effective mechanical properties, homogenization, microstructure, porosity, residual stress

1 | INTRODUCTION

Powder bed fusion (PBF) is one of the most popular additive manufacturing (AM) technologies enabling innovation in the design of industrial products and bringing revolution to the series production of them [23,37,43]. Distinguished from the other compositions in the category of PBF, selective sintering (SS) binds the powder bed driven via a scan of an energy beam (mostly a laser beam or an electron beam) layer-wisely without creating a significant melt pool, which usually results in a high product porosity [13,27,55]. Therefore, SS has been applied for industrial production in manufacturing porous structures, especially medical scaffold and bones [10,45,50]. It is also feasible in producing components in which

Abbreviations: PBF, powder bed fusion; RVE, representative volume element; SS, selective sintering.

the materials have relatively high melting/transition temperature [13,22,25] or request relatively low process temperature in order to avoid the material transitions [17,42].

Microstructure and its evolution during the PBF essentially bridge the process parameters, majorly the power as well as the scan speed of the beam, and the preheating temperature, to the end-up performance of manufactured components [1,36,53]. Although experimental methods regarding insitu and real-time characterization maintain lasting high interests, modeling and simulation methods play a crucial role in exploring the process-microstructure-property relation and thereby form the backbone of the correlation studies [23,30,53,55,56,59]. This enables the direct linkage between the process parameters and the resultant microstructure, which influences largely the performance of the final product, by providing clear-defined underlying physics. In the sense of tailoring size, distribution, and morphology of pores in a functional porous structure, it specifically requires the detailed tracing of nonisothermal transient microstructure on the mesoscale (i.e., $0.1 \sim 100$ μm [34]) as a result of interactive underlying physics, that is, the mass and thermal transfer, coalescence as well as the grain growth , and even the partial melting of the particles. These requirements can be fulfilled by phase-field method among the existent approaches. In our latest work, we proposed a thermodynamically consistent nonisothermal phase-field model for selective sintering, which recapitulated processes during SS, such as a temperature field with a high gradient, mass transfer through partial melting as well as diffusion, and particle/grain necking as well as coarsening [55]. 3D simulations with a mesoscopic powder bed geometry were also performed and ready for further calculation of the end-up mechanical properties.

On the other hand, with increasing and widespread attractions on tomographic characteristic methods, in which phase-field method has shown its compatibility and robustness in reconstructing such characterizations with smoothed (diffusive) interfaces [2,20,44], it is also interesting to perform accurate property calculations directly on a microstructure with diffusive interfaces rather than conducting extra steps of determining the sharp interfaces from the characterized microstructure [35]. There are generally two schemes to simulate the mechanical behavior on nonisothermal transient microstructure: the coupled and segregated schemes. The coupled scheme considers explicitly the interaction between the mechanical dynamics as well as thermal-/microstructure evolution. This scheme causes the entanglement between the temperature and mechanical fields [33], and thus is time and resource consuming. Therefore, the segregated (or weakly coupled) scheme is widely used in the current research [29], in which the thermal stress is calculated based on the resultant microstructure with temperature field from the phase-field simulation, neglecting the reaction from the mechanics on the thermal-/microstructure evolution.

Most of the mechanical analysis focuses on understanding the formation of residual stress during metal PBF. The residual stress depends on the process parameters, such as scanning orientation, beam power, and scan speed. A few single layer models were developed to study the influence of process parameters on the residual stress [16,38,48,56]. To further include the cumulative component level of stress state in a multilayer structure, models with multiple thin layers were developed to study residual stress and distortion of the structure. The multilayer model tends to quantitatively explain the residual stress and distortion observed in experiments. For example, Williams et al. [51] predicted the distortion within only 10% difference compare to the experimental measurement. The multilayer and multitrack model developed by Ren et al. [40] is used to not only explain the experimental observation of residual stress but also to study the reduction of distortion in additive manufacturing, where the simulation of the thermal stress uses a simplified homogeneous model. To predict the deflection and residual stress of components manufactured with PBF at large-scale, part-scale multilayer models were developed [4,6,11]. The simulation of the part-scale model uses layers around 1 mm [11]. At this scale, the simplified homogeneous model is used not only in the thermo-mechanical analysis, but also in the simulation of the thermal profiles of the powder bed [6]. Since PBF-manufactured components with complex geometry are considered in these models, generation of the analysis-suitable mesh can also be problematic. Finite cell method instead of the finite element method was adopted to simulate the PBF process at part-scale by means of a layer-by-layer activation process [4]. Few works directly considered mechanical analysis of the multilayer porous microstructure on the mesoscale, such as porous 316L stainless steel fabricated by SS [52]. With increasing computation resources, a direct investigation of multilayer finite element simulation of microstructure during the SS process is possible and can give an in-depth insight into the formation of residual stress.

By combining phase-field simulations, computational homogenization and thermo-mechanical analysis in the finite element method, we present a comprehensive numerical study on the process-microstructure-property relation of SS-processed 316L (SS316L). In particular, the microstructure and the transient thermal history were firstly calculated by using the proposed nonisothermal phase-field model. They were subsequently transferred to the FE-based homogenization and thermo-mechanical FE simulations, in order to evaluate the effective elastic properties and the thermal residual stress. Thereby multilayer simulations based on an efficient scheme of layer-wise powder deposition were employed to

generate representative volume elements (RVE) of sufficient large size. Using the proposed numerical scheme, massive simulations have been carried out with varying beam power and scan speeds. The obtained large amount of data were analyzed to unveil the influence of the process parameters on the porosity, the effective elastic properties and the residual stress.

2 | THEORETICAL MODELS

Assuming heat transfer, strongly dependent on the transient microstructure, is weakly coupled with mechanics, a subsequent scheme is employed in this work, that is, the nonisothermal phase-field simulation for the coupled thermal-/microstructure evolution and a subsequent thermo-mechanical simulation for the thermal stress and deformation of the microstructure.

2.1 | Nonisothermal phase-field model of SS processes

Starting from a Ginzburg–Landau-type entropy density functional, the authors have developed a nonisothermal phase-field model for simulation of the microstructure evolution and the thermal history during the SS process [55]. For the sake of completeness, the model is briefly summarized here. Thereby both conserved and nonconserved order parameters (OPs) are employed to represent the polycrystalline metallic materials. The conserved OP ρ indicates the substance (incl. unmelted and partially melted region), while the nonconserved OPs $\{\eta_i\}$, $i = 1, 2, \ldots$ distinguish particles with different crystallographic orientations. The numerical constraint $\sum_i \eta_i + (1 - \rho) = 1$ allows $\{\eta_i\}$ to be valued only when $\rho = 1$, that is, grains only exist in the substance. A free energy functional $\mathscr{F}$, depending on OPs and the local temperature field T, is derived as

$$\mathscr{F}(T, \rho, \{\eta_i\}) = \int_\Omega \left[f(T, \rho, \{\eta_i\}) + \frac{1}{2} T \kappa_\rho |\nabla \rho|^2 + \frac{1}{2} T \kappa_\eta \sum_i |\nabla \eta_i|^2 \right] d\Omega, \tag{1}$$

where the local free energy density is constructed in the form of a Landau polynomial as

$$f(T, \rho, \{\eta_i\}) = \xi \left(\underline{A}\rho + \underline{B} \sum_i \eta_i \right) f_{\mathrm{ht}}(T) + \underline{C}(T) \left[\rho^2 (1 - \rho)^2 \right]$$

$$+ \underline{D}(T) \left[\rho^2 + 6(1 - \rho) \sum_i \eta_i^2 - 4(2 - \rho) \sum_i \eta_i^3 + 3 \left(\sum_i \eta_i^2 \right)^2 \right]. \tag{2}$$

with

$$f_{\mathrm{ht}}(T) = c_{\mathrm{r}} \left[T \ln \frac{T}{T_0} - (T - T_0) \right],$$

$$\underline{C}(T) = \underline{C}_{\mathrm{pt}} - \underline{C}_{\mathrm{cf}}(T - T_0),$$

$$\underline{D}(T) = \underline{D}_{\mathrm{pt}} - \underline{D}_{\mathrm{cf}}(T - T_0).$$

In this formulation, multiple minima are presented including $(\rho = 0, \{\eta_1 = 0, \eta_2 = 0, \ldots, \eta_N = 0\})$ for an atmosphere/pore state and $(\rho = 1, \{\eta_1 = 1, \eta_2 = 0, \ldots, \eta_N = 0\})$, $(\rho = 1, \{\eta_1 = 0, \eta_2 = 1, \ldots, \eta_N = 0\})$, ... , $(\rho = 1, \{\eta_1 = 0, \eta_2 = 0, \ldots, \eta_N = 1\})$ for grain states with different orientations. Model parameters $\underline{C}_{\mathrm{pt}}$, $\underline{D}_{\mathrm{pt}}$, $\underline{C}_{\mathrm{cf}}$, and $\underline{D}_{\mathrm{cf}}$ are related to the barrier heights between minima with the subscript "pt" and "cf" denote the contribution from the potential term or the configurational term, respectively. Heat term f_{ht} tilts the "multiwell" due to the local heat variation in certain phase, manifesting the variable thermodynamic stability due to the change of local thermal conditions. T_0 is an arbitrary temperature serving as the upper-bound reference temperature where parameters $\underline{C}_{\mathrm{pt}}$ and $\underline{D}_{\mathrm{pt}}$ are determined. Model parameters $\underline{A}$, $\underline{B}$, $\underline{C}$, and $\underline{D}$ as well as gradient constants κ_ρ and κ_η can be obtained by fitting the experimental temperature-dependent surface and grain boundary energy $\gamma_{\mathrm{sf}}(T)$ and $\gamma_{\mathrm{gb}}(T)$ with a given diffusive interface, where the coefficient ξ is employed to adjust the heat contribution f_{ht} to the interface in order to favor the multivariable regression (see Supplementary Note 1 of [55]).

Following our previous investigations [53–55], the kinetic of ρ is governed by the Cahn–Hilliard equation as

$$\dot{\rho}(\mathbf{r}, t) = \nabla \cdot \left[M \nabla \left(\frac{\partial f}{\partial \rho} - T \kappa_\rho \nabla^2 \rho \right) \right] \tag{3}$$

with the isotropic diffusive mobility formulated to consider not only contributions from mass transfer paths through substance, atmosphere, surface, and grain boundary [49,53–55], but also the diffusion enhancement due to possible partial melting [55], that is,

$$M = \frac{1}{2 \left(\underline{C} + \underline{D} \right)} \left[\Phi_{ss} D_{ss} + \Phi_{at} D_{at} + \Phi_{sf} D_{sf} + \Phi_{gb} D_{gb} \right] + \Phi_M(T) M_{melt}, \tag{4}$$

where D_{path} is the effective diffusivity of the mass transport via path = ss, at, sf, gb, and Φ_{ss}, Φ_{at}, Φ_{sf}, and Φ_{gb} are also interpolating functions to indicate substance (including solid and liquid), atmosphere/pore, surface and grain boundary, respectively, which obtain unity only in the corresponding region. They can be simply formulated as

$$\Phi_{ss} = \rho^3 \left(10 - 15\rho + 6\rho^2 \right), \quad \Phi_{at} = 1 - \rho^3 \left(10 - 15\rho + 6\rho^2 \right),$$
$$\Phi_{sf} = 16\rho^2(1 - \rho)^2, \quad \Phi_{gb} = 16 \sum_{i \neq j} \eta_i^2 \eta_j^2.$$

Notice that such formulation holds only when a limited melting phenomenon is assumed to occur around the surface of particles. In this regard, the contribution of the partial melting is treated more like an enhanced surface diffusion when $T \rightarrow T_M$. It is worth noting that the formulations in Equations 3-4 disregard the detailed melt flow dynamics as well as contributions from intercoupling between mass and heat transfer.

As for kinetic for $\{\eta_i\}$, the Allen–Cahn equation is directly utilized, which is also the reduced from [54] without temperature-gradient-driven grain boundary (GB) migration.

$$\dot{\eta}_i = -L \left(\frac{\partial f}{\partial \eta_i} - T_0 \kappa_\eta \nabla^2 \eta_i \right). \tag{5}$$

Here L can be explicitly formulated by using the GB mobility G_{gb}, GB energy $\gamma_{gb}^{T_0}$ and the gradient model parameter κ_η as

$$L = \frac{G_{gb} \gamma_{gb}^{T_0}}{T_0 \kappa_\eta}. \tag{6}$$

It should be noted that the gradient model parameter of Equation 6 has been modified from the original equation in [32] to $T\kappa_\eta$ for the physical coherence.

Finally, for the heat transfer equation, we have derived a heat transfer kinetic coupled with terms with transient OPs, showing the latent heat brought by the microstructure evolution

$$c_r \dot{T}(\mathbf{r}, t) + \frac{\partial e_{pt}}{\partial \rho} \dot{\rho}(\mathbf{r}, t) + \sum_i \frac{\partial e_{pt}}{\partial \eta_i} \dot{\eta}_i(\mathbf{r}, t) = \nabla \cdot (\mathbf{k} \cdot \nabla T) + q(\mathbf{r}, t). \tag{7}$$

with a temperature-independent potential landscape e_{pt} as

$$e_{pt}(\rho, \{\eta_0\}) = \underline{C}_{pt} \left[\rho^2(1 - \rho)^2 \right] + \underline{D}_{pt} \left[\rho^2 + 6(1 - \rho) \sum_i \eta_i^2 - 4(2 - \rho) \sum_i \eta_i^3 + 3 \left(\sum_i \eta_i^2 \right)^2 \right],$$

and the thermal effect incited by the beam is equivalently treated as a volumetric heat source with its distribution along the depth direction formulated in a radiation penetration fashion, as the powder bed is regarded as an effective homogenized optical medium, that is,

$$q(\mathbf{r}, t) = P p_{xy}[\mathbf{r}_O(\mathbf{v}, t)] \frac{da}{dz},$$

in which the in-plane Gaussian distribution p_{xy} with a moving center $\mathbf{r}_O(\mathbf{v}, t)$. P is the beam power and $\mathbf{v}$ is the scan velocity with its magnitude $v = |\mathbf{v}|$ as the scan speed, which are two major processing parameters in this work. The absorptivity profile function along depth $\mathrm{d}a/\mathrm{d}z$ which is calculated based on [14,55].

It is obvious that when one ignores the effects of those latent heat induced by microstructure evolution (i.e., the evolution of the pore/substance as well as unique grains), Equation (7) can be degenerated to the conventional Fourier's equation for heat conduction with an internal heat source. In this work, the spatial distribution of $\mathbf{k}$ within the system is treated similarly as the diffusive mobility in Equation (4), yet only $\mathbf{k}$ on the substance (ss) and atmosphere/pores (at) are specifically distinguished, that is,

$$\mathbf{k} = \mathbf{k}_{ss} + \mathbf{k}_{at}, \tag{8}$$

with

$$\mathbf{k}_{ss} = k_{ss}\Phi_{ss}\mathbf{I}, \quad \mathbf{k}_{at} = k_{at}\Phi_{at}\mathbf{I}.$$

2.2 | Mechanical analysis

RVEs with simulated microstructure are then subjected to thermo-mechanical analysis and computational homogenization based on the finite element approach. Therefore, in this and the following subsection, the related equations are summarized. Consider the microstructure in the domain Ω surrounded by the boundary $\partial\Omega$. Assuming the quasi-static problem with small strain approximation, the microstructure is governed by the stress equilibrium

$$\nabla \cdot \boldsymbol{\sigma} = \mathbf{0} \quad \text{in } \Omega, \tag{9}$$

where $\boldsymbol{\sigma}$ is the stress tensor, $\mathbf{0}$ represents the null vector, and the body force is ignored. For heterogeneous microstructures, the anisotropic constitutive relation is given as

$$\boldsymbol{\sigma} = \mathbf{C} : (\boldsymbol{\varepsilon} - \boldsymbol{\varepsilon}_0), \tag{10}$$

where $\mathbf{C}$ is the stiffness tensor, the total strain $\boldsymbol{\varepsilon}$ is defined as the symmetric part of the displacement gradient $\nabla\mathbf{u}$

$$\boldsymbol{\varepsilon} = \frac{1}{2}\left(\nabla\mathbf{u} + \mathbf{u}\nabla\right). \tag{11}$$

For a general elasto-plastic thermo-mechanical problem, the eigenstrain $\boldsymbol{\varepsilon}_0$ contains both the plastic strain and thermal strain. In this article, only the thermal strain is considered and it is defined as

$$\boldsymbol{\varepsilon}_0 = \alpha(T - T_0)\mathbf{I}, \tag{12}$$

where α is the temperature dependent coefficient of thermal expansion and $\mathbf{I}$ is the identity tensor.

The stress equilibrium is subjected to either displacement or traction boundary condition

$$\mathbf{u} = \overline{\mathbf{u}} \quad \text{or} \quad \boldsymbol{\sigma} \cdot \hat{\mathbf{n}} = \overline{\mathbf{t}} \quad \text{on } \partial\Omega, \tag{13}$$

where $\overline{\mathbf{u}}$ is the prescribed displacement on the boundary, $\hat{\mathbf{n}}$ is the normal vector of the boundary, and $\overline{\mathbf{t}}$ is the applied traction on the boundary.

As it is explained in more details later, the resultant porous structure from phase-field simulation is mapped to a uniform finite element mesh with phase-dependent elastic properties. The variation of material properties across the diffusive interface is influential to the mechanical result. Therefore, appropriate spatial interpolation of the mechanical properties is necessary. In this preliminary simulation work on SS316L, isotropic mechanical properties are considered. In particular, the Young's modulus and the Poisson's ratio, of the resultant microstructure are employed in the direct interpolation scheme as employed in microstructure simulations (Equations (4) and (8)), that is,

$$E(\rho^J) = E_{ss}\Phi_{ss}(\rho) + E_{at}\Phi_{at}(\rho), \quad \nu(\rho) = \nu_{ss}\Phi_{ss}(\rho) + \nu_{at}\Phi_{at}(\rho) \tag{14}$$

in which E_{ss} and ν_{ss} are respectively the Young's modulus and the Poisson's ratio of the SS316L substance, while E_{at} and ν_{at} are of the atmosphere, respectively. $E_{at} = 0.01$ MPa and $\nu_{at} = 0$. The interpolation functions $\Phi_{ss}(\rho)$ and $\Phi_{at}(\rho)$ use the same formulation as Equation (4).

Note that the interpolation can be also made on bulk and shear modulus (K and G), which are two independent elastic constants of an isotropic stiffness tensor. Interpolation directly on the stiffness [26,57] or stress [7,19] are also employed in coupling problems of phase-field and mechanics, which are essentially equivalent to the direct interpolation in K and G as shown in Equation (19). The difference between interpolation on E and ν as well as K and G has been rarely discussed would be addressed in the upcoming work. Other interpolation schemes, such as the inverse interpolation scheme proposed in [35], with their corresponding physical standpoint and numerical outcome should also be investigated.

2.3 | Computational homogenization analysis

The microstructure obtained in multilayer phase-filed simulations is used as an RVE. To evaluate the effective properties of the microstructure, we adopt the ideas of homogenization for the linear elasticity [41,46]. Based on the Hill's criterion, three kinds of boundary conditions can be applied: linear displacement boundary conditions, uniform traction boundary conditions, or the related periodic boundary conditions. In the phase-field simulation, the boundary condition is not periodic and thus the simulated microstructure is not periodic. Therefore, the periodic boundary condition for homogenization is inappropriate. Considering the fact that the Young's modulus of the atmosphere is very small (0.01 MPa) compared to the powders (180 GPa), it can lead to convergence difficulty when the traction boundary condition is applied. Hence, the linear displacement boundary condition is chosen for homogenization, which is defined as

$$\mathbf{u} = \boldsymbol{\varepsilon}_0 \cdot \hat{\mathbf{x}} \quad \text{on } \partial\Omega, \tag{15}$$

where $\hat{\mathbf{x}}$ is coordinates on the boundaries, and the constant tensor $\boldsymbol{\varepsilon}_0$ represents the macroscopic strain. As the average strain theorem shows,

$$\langle\boldsymbol{\varepsilon}\rangle = \frac{1}{2V}\int_\Omega (\nabla\mathbf{u} + \mathbf{u}\nabla)d\Omega = \frac{1}{2V}\int_{\partial\Omega}(\mathbf{u}\otimes\hat{\mathbf{n}} + \hat{\mathbf{n}}\otimes\mathbf{u})dS = \frac{\boldsymbol{\varepsilon}_0}{2V}\cdot\int_{\partial\Omega}(\hat{\mathbf{x}}\otimes\hat{\mathbf{n}} + \hat{\mathbf{n}}\otimes\hat{\mathbf{x}})dS = \boldsymbol{\varepsilon}_0, \tag{16}$$

where V is the volume of the RVE. After solving the mechanics problem of the RVE under the given linear displacement condition, the stress distribution inside the RVE can be obtained. Thus the volume average stress in the RVE, which corresponds to the macroscopic stress, is evaluated as

$$\langle\boldsymbol{\sigma}\rangle = \frac{1}{V}\int_\Omega \boldsymbol{\sigma}d\Omega. \tag{17}$$

Then the effective stiffness tensor of the RVE can be calculated using the relation

$$\langle\boldsymbol{\sigma}\rangle = \mathbf{C}_{\text{eff}} : \langle\boldsymbol{\varepsilon}\rangle. \tag{18}$$

Note that in the computational homogenization, to obtain the effective stiffness tensor of a three-dimensional RVE, six independent loading scenarios are simulated: normal stretching test along each of three Cartesian directions and shearing test in each of three Cartesian coordinate planes. The average stress calculated with each boundary condition can be used to calculate one column of the effective stiffness tensor $\mathbf{C}_{\text{eff}}$.

In powder-bed based additive manufacturing, anisotropic porous structure and thus anisotropic effective elasticity can be expected, particularly the orthogonal feature w.r.t. the building direction. In practice, by limiting for example, the powder bed thickness of the single scan (around two layers of powders), the anisotropy can be avoided to a certain extent. This has been regarded in the phase-field microstructure simulation. Thus, the resultant stiffness tensors are nearly isotropic and can be characterized by the isotropic elastic constants. For instance, the isotropic constitutive relation can be given as

$$\boldsymbol{\sigma} = K\varepsilon^{\text{tr}}\mathbf{I} + 2G\mathbf{e}, \tag{19}$$

where K is the bulk modulus, G is the shear modulus, $\varepsilon^{\text{tr}} = \text{tr}(\varepsilon)$ represents the trace of the strain tensor, and $\mathbf{e} = \varepsilon - \varepsilon^{\text{tr}}\mathbf{I}/3$ is the deviatoric strain tensor. Consider the superposition of linear elasticity, and denote $\tilde{\boldsymbol{\sigma}}$ and $\tilde{\boldsymbol{\varepsilon}}$ to be the sum of the

stress field and strain field obtained with six boundary conditions, respectively. Then the effective bulk modulus $\tilde{K}$ and effective shear modules $\tilde{G}$ can be evaluated as

$$\tilde{K} = \frac{\tilde{\sigma}^{\mathrm{tr}}}{3\tilde{\varepsilon}^{\mathrm{tr}}}, \quad \tilde{G} = \frac{\tilde{\mathbf{e}} : \tilde{\mathbf{s}}}{2\tilde{\mathbf{e}} : \tilde{\mathbf{e}}}, \tag{20}$$

where $\tilde{\sigma}^{\mathrm{tr}}$ is the trace of the stress tensor, and $\tilde{\mathbf{s}} = \tilde{\sigma} - \tilde{\sigma}^{\mathrm{tr}}\mathbf{I}/3$ is the deviatoric stress tensor. With the effective bulk modules and shear modules, the effective Young's modulus and Poisson's ratio can be obtained as

$$\tilde{E} = \frac{9\tilde{K}\tilde{G}}{3\tilde{K} + \tilde{G}}, \quad \tilde{\nu} = \frac{3\tilde{K} - 2\tilde{G}}{2(3\tilde{K} + \tilde{G})}. \tag{21}$$

For more details of homogenization in the linear elasticity, one can refer to [46].

3 | SIMULATION SETUP

3.1 | Finite element implementation

The models are numerically implemented by finite element method (FEM) within the simulator "NIsoS" developed by authors based on MOOSE framework [47]. 8-node hexahedron Lagrangian elements are chosen to mesh the geometry. Transient solver with preconditioned Jacobian-Free Newton-Krylov method (PJFNK) and backward Euler algorithm has been employed for both problems. For nonisothermal phase-field simulations, the Cahn–Hilliard equation in Equation (3) is solved in a split way [9,53–55,58]. Adaptive meshing and time stepping schemes are used to reduce computation costs. The constraint of the order parameters is fulfilled using the penalty method. For mechanical analysis, the resultant OP and temperature landscapes from the nonisothermal phase-field simulation are mapped onto a uniform mesh with the mesh size of $60 \times 60 \times 60$, and then used to interpolate the nonuniform distribution of material parameters. Dirichlet boundary conditions are applied for the estimation of the effective mechanical properties and calculation of residual stress. The large-scale parallel CPU computations for each simulation domain, which has DOFs on the order of 10 000 000 for both nonlinear system and auxiliary system, are performed with 72 processors and 2 GByte RAM per processor based on OpenMPI. Each simulation consumes on the order 10 000 core h.

Table 1 gives the material properties and size distribution and powder properties (incl. the mean diameter $\bar{d}$ with the corresponding standard deviation s_d and the cut-off diameter d_{cut}) of SS316L powders in the argon atmosphere following our previous work [55]. $\mathfrak{R}$ in the table represents the ideal gas constant.

3.2 | 3D-multilayer simulation scheme

Figure 1 depicts the scheme of the 3D-multilayer SS simulation, including two major stages. In the microstructure simulation stage, it can further separated into four steps as shown in Figure 1A. In short, SS316L powders are firstly deposited into a 250 μm × 250 μm × 250 μm cubic domain under a given gravitational force using grain piling software (e.g., GrainGeo module from the commercial software GeoDict®). After the deposition, the center coordinate and radius of each unique powder are recorded as a vertex of an adjacency network generated according to given adjacency distance. In order to enhance the computational efficiency of phase-field finite simulation, the Welsh–Powell algorithm and the grain tracking are performed on the network to find the optimized assignment of OPs $\{\eta_i\}$ among the powders, that is, near-least of $\{\eta_i\}$ is assigned, meanwhile powders assigned with the same OP η_i are sufficiently distanced to avoid possible coalescence [55]. Next, those powders are imported into the simulator as the initial conditions for correspondingly assigned OP η_i and, eventually, perform the phase-field simulation. After finishing the simulation of a layer, this resultant microstructure is voxelized and imported back into the grain piling software, then perform the deposition of the next powder layer. These four steps are repeated until the objective layer number (or height) is reached. In this article, we printed three layers as shown in Figure 1B, because the preliminary study demonstrates that the resultant size of the RVEs is sufficient to be statistically representative. Once a microstructure simulation finishes, the resultant spatial distribution of the substance and temperature is directly mapped as the nodal value (denoted as ρ^J and T^J) from an adaptive mesh to a uniform mesh to perform the mechanical analysis of the next stage, including the computational homogenization as

TABLE 1 Material properties and size distribution of the SS316L powders used in simulations

	Properties	Expressions (T in K)	Units	References
Nonisothermal phase-field	T_M	~ 1700	K	
	D_sf	$0.40 \exp\left(-2.200 \times 10^5/\Re T\right)$	m²/s	[3]
	D_gb	$2.40 \times 10^{-3} \exp\left(-1.770 \times 10^5/\Re T\right)$	m²/s	[3]
	D_ss	$2.17 \times 10^{-5} \exp\left(-2.717 \times 10^5/\Re T\right)$	m²/s	[31]
	G_gb	$3.26 \times 10^{-3} \exp\left(-1.690 \times 10^5/\Re T\right)^\mathrm{a}$	m⁴/(J s)	
	M_melt	$\sim 3.45 \times 10^{-13}$ [b]	m⁵/(J s)	
	k_ss	$10.292 + 0.014T$	J/(s m K)	[28]
	k_at	~ 0.06	J/(s m K)	[15]
	c_ss	$3.61 \times 10^6 + 1272T$	J/(m³ K)	[28]
	c_at	717.6	J/(m³ K)	[5]
	$\mathscr{L}_\mathrm{ss}$	2.4×10^9	J/m³	[28]
Thermal Mechanics	E_ss	180^c	GPa	[18]
	ν_ss	0.3^c	-	[18]
	α_ss	0.019^c	1/K	[18]
Powder size distributions	$\bar{d}$	35	μm	
	s_d	10	μm	
	d_cut	15	μm	

[a]Activation energy is obtained from [8] while the prefix factor is estimated as unity at T_M after normalization.
[b]Estimated as $100D_\mathrm{sf}/2(\underline{C} + \underline{D})$.
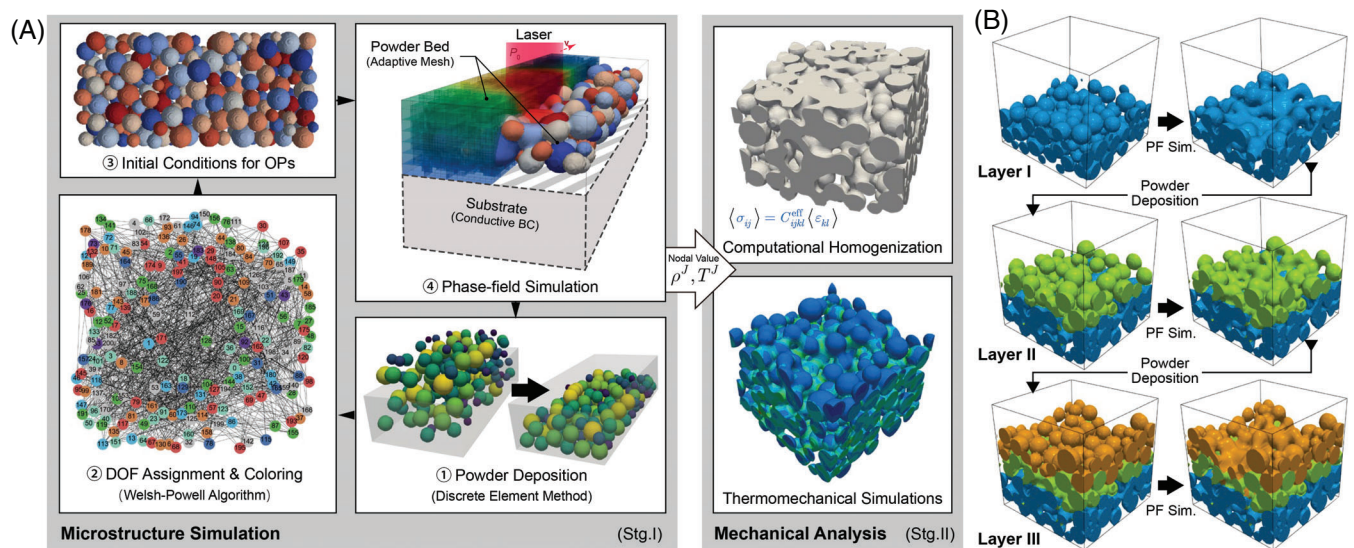[c]Obtained at 293 K.

FIGURE 1 (A) Schematics of 3D-multilayer SS simulations of microstructure and mechanical properties. Four steps in the microstructure simulation (Stage I) are labeled. (B) The workflow of the 3D three-layer SS simulation performed in this work

well as thermo-mechanical simulations. This is achieved by employing the MOOSE-embedded `SolutionUserObject` class and associated functions.

The aforementioned simulation scheme is proposed for general cases involving the needs of concerning polycrystalline structure and properties, which would considerably build up the computational assumption to the numerical calculations. Focusing solely on porous structure and related mechanical properties, only one grain orientation (i.e., one η) was employed, meaning the "OP Assignment & Coloring" step was tentatively skipped in this article. Systematic investigations on influences from the polycrystalline structure will be covered in our upcoming works.

4 | RESULTS AND DISCUSSION

4.1 | Morphology and porosity under varying process parameters

We firstly performed a series of 3D-multilayer phase-field simulations on the microstructure of SS processed samples varying pairs of beam power and scan speed (hereinafter as *P-v* pairs) in order to investigate the dependence of resultant morphology and porosity on the selection of *P-v* pair. The morphology and corresponding absolute porosity φ of selected *P-v* pairs are presented in Figure 2, which can be roughly divided into two groups. From A_2 to A_4, the scan speed v is fixed at 100 mm/s while the beam power P is sequentially increased from 15 to 30 W. From A_5 to A_7, on the other hand, v is sequentially decreased from 150 to 75 mm/s while fixing P at 20 W. Both groups show the variation of resultant
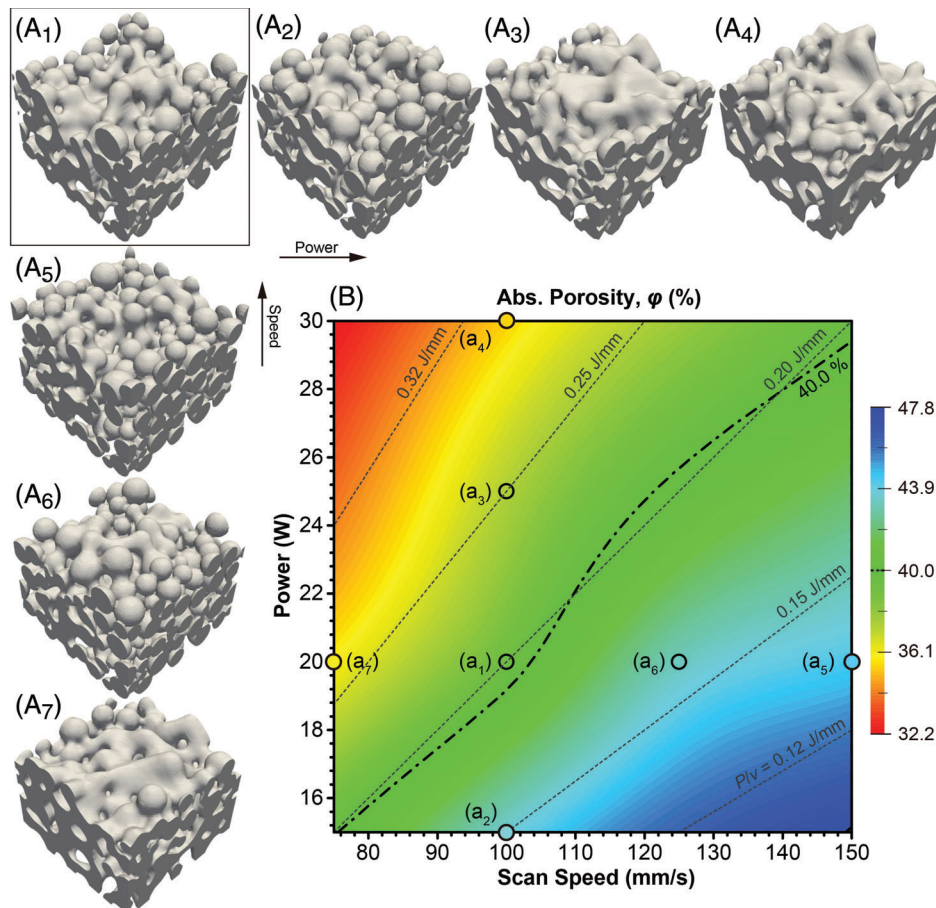

FIGURE 2 (A_1)–(A_7) Morphologies of SS processed three-layer powder bed with varying beam power and scan speed. Corresponding *P-v* sets are also denoted as points in the absolute porosity map in (B). The dash-dotted line in (B) is the median isoline (40%) of the resultant porosity

microstructure from less-bound powders to continuous pieces with smooth surface morphology, implying an enhanced partial melting. It demonstrates that both increasing beam power and decreasing scan speed can improve the densification of the powder bed via enhancing partial melting. This effect can be also reflected in the reduction of the porosity, which drops from 44.4% to 36.1% for the scan speed decrease from 150 to 75 mm/s at beam power of 20 W, and from 43.5% to 35.5% for the beam power increase from 15 to 30 W at a scan speed of 100 mm/s. Due to the monotonic relation of φ to P and v respectively within the testing P-v plane, that is, monotonic reducing φ with both increasing P and decreasing v, we thereby perform the thin plate spline (TPS) extrapolation of φ over the testing P-v plane, as shown in Figure 2B. The distribution over P-v plane presents a similar pattern as the one examined on the single layer in [55], yet it might be suffered from issues due to insufficient sampling, such as over-fitting, which requires further investigation with adequate sample size in the follow-up works.

It should be also noted that before the calculation of this overall absolute porosity the simulated sample should be subject to a virtual polishing, in order to remove the surface effect. As indicated by Figure 3A$_2$, the surface roughness on the last printed layer differ from the pore morphology in the region of previous layers, which has experienced multi-rounds of scanning and becomes dense. We virtually polish the simulated sample by a height ΔH, while denote the left sample height by H_R. The choice of ΔH is according to the segment-wise calculation along the scan direction (SD) and the building direction (BD) and the convergence of the calculated porosity shown in Figure 3B. Note that the cross sectional porosity along the scanning direction varies much less, indicating that the size of the RVE in the respective direction is sufficient.

Even though preferred in porosity reduction, a SS process with either high beam power or low scan speed is not applicable in the practical manufacturing. Taking some of the mostly addressed disadvantages for instance, a high beam power would lead to large energy consumption and intensified powder scattering with its following side-effects [21], while a low scan speed would significantly delay the manufacturing process. It thus raises interest in optimizing the porosity control via the P-v pair, in this regard the potential relation between porosity and P-v pair is in demand. As divided by the porosity median 40.0% in the Figure 2B, the P-v pair located at the lower-right region leads to limited partial melting and thus higher porosity, while the upper-left region leads to significant partial melting (or even full melting) and thus lower porosity, revealing a possible allometric relation $\varphi \propto P^{-m}v^{n}$ with positive-defined indices m and n. However, the porosity seems not uniquely dependent on the specific energy (proportional to P/v)—a widely accepted porosity identifier, since the porosity contours are apparently not parallel to the isoline of P/v (Figure 2B), which has also been revealed both numerically [53,55] and experimentally [39]. This requires further assistance from the data-driven statistical methods, such as multivariable frequentist or Bayesian approaches.
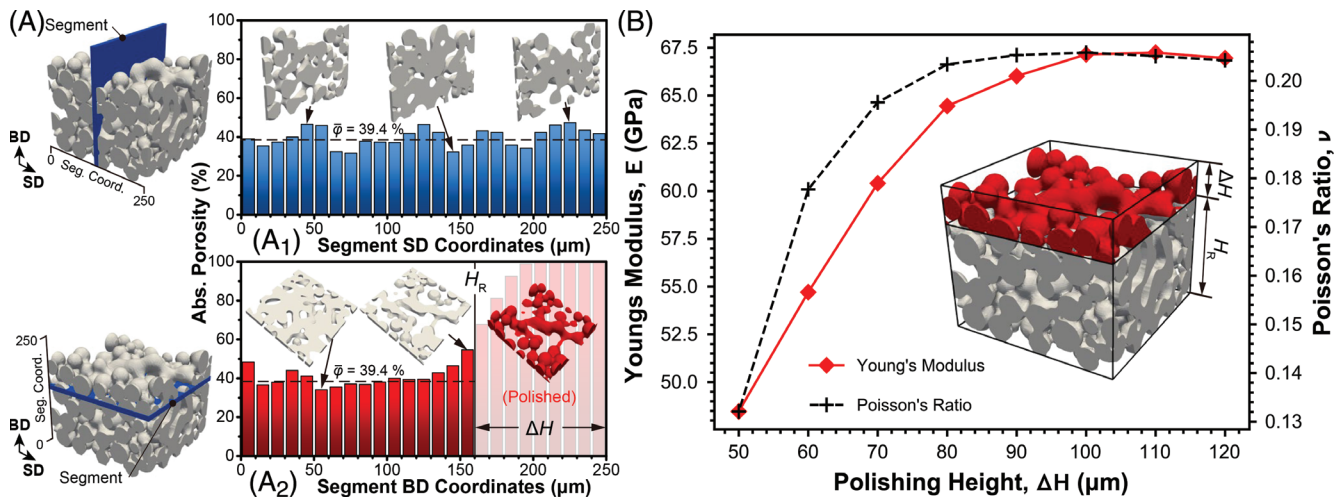

FIGURE 3 (A) Segment-wise porosity histogram of the sample produced under 20 W-100 mm/s along (A$_1$) scan direction (SD) and (A$_2$) building direction (BD) with chosen reference height H_R as well as polishing height ΔH denoted. (B) Convergence study in estimation of the effective mechanical properties of a RVE with different ΔH

4.2 | Effective mechanical properties

Different process parameters result in different morphology of the microstructure and thus different mechanical properties of the RVE. In this subsection, we show the dependence of the effective elastic properties on the process parameters.

As explained in the last section, near the top surface of the as-simulated microstructure the cross-sectional porosity is larger than that in the interior region. Therefore, the surface "polishing" by cutting off the top surface of height ΔH is needed, as shown in the inset of Figure 3B. The thickness of the polishing layer ΔH, in other words the remaining height H_R in the x_3 direction has large influence on the elastic stiffness in the x_3 direction.

Take the case of the beam power of 20 W and the scan speed of 100 mm/s as an example. For a polishing thickness of $\Delta H = 70$ μm, in other words $H_R = 180$ μm, the calculated effective stiffness matrix is

$$\mathbf{C}_{\text{eff}} = \begin{bmatrix} 6.63 & 1.88 & 1.70 & 0.00 & -0.07 & 0.07 \\ 1.88 & 6.67 & 1.73 & -0.08 & -0.01 & 0.04 \\ 1.70 & 1.73 & 6.09 & -0.04 & -0.07 & 0.03 \\ -0.02 & -0.07 & -0.02 & 2.55 & 0.02 & -0.01 \\ -0.02 & -0.01 & -0.05 & 0.03 & 2.52 & 0.01 \\ -0.03 & -0.11 & -0.00 & -0.02 & 0.02 & 2.62 \end{bmatrix} \times 10^4 \text{ MPa.} \tag{22}$$

It is noticeable that the component C_{33} is around 10% smaller than C_{11}. The anisotropy can be due to the layered wise building of the RVE. In the simulations, every newly deposited powder bed consists of about two layers of powders, and it should be appropriate to minimize the anisotropy. On the other hand, this anisotropy can also result from the surface roughness in the top layer, as demonstrated in Figure 3A$_2$. To investigate this, we increase the thickness of the polishing layer ΔH. Figure 3 shows the dependence of effective Young's modulus on the polishing height ΔH. It can be seen that the estimated Young's modulus and Poisson's ratio converge after $\Delta H = 100$ μm with corresponding RVE height of $H_R = 150$ μm. The relative difference of Young's modulus compared to the convergent value is less than 0.3%, and the difference between C_{11} and C_{33} becomes negligible. It should be noted that the requested polishing height depends on the processing parameters, in particular the level of partial melting of the powders. Therefore, the appropriate height for estimation of the effective mechanical properties varies with process parameters. In the following, we use $H_R = 150$ μm which guarantees that the surface roughness is removed for all simulated microstructure.

Figure 4A shows the variation of effective mechanical properties with respect to different beam powers at the same scan speed of 100 mm/s. With the increasing beam power, the effective Young's modulus and the Poisson's ratio increase around 5.5% and 9.0% (normalized w.r.t. the bulk values, i.e., E_{ss} and ν_{ss}), respectively. This increment is due to an increase of density (or decrease of porosity) of the RVE at a high beam power with high degree of partial melting. It can also be seen that the relationship between the effective mechanical property and beam power is nonlinear, where the slope of the curves decreases with increasing beam power. This indicates the effective mechanical properties slowly convergent to the mechanical properties of bulk stainless steel at high beam power. Similar results are found for different scan speeds at the same beam power of 20 W. Since the small porosity is observed with a small scan speed, larger effective properties are observed with decreasing scan speed. With decreasing scan speed, the effective Young's modulus and the Poisson's ratio increase around 8.0% and 8.5% (normalized w.r.t. the bulk values), respectively. The decreasing of the effective properties slows down at higher scan speed. This is because the partial melting of the powder is very small and the morphology of the microstructure is almost unchanged at a high scan speed, where the porosity of the RVE converges to initial porosity without partial melting. As a consequence, the effective properties also converge to the initial effective properties of the RVE without partial melting.

As discussed above, both cases show nonlinear relation between process parameter and effective mechanical properties. Different process parameters result in different morphology of the microstructure and different porosity. Although it is not straightforward to estimate the influence of morphology of the microstructure on the effective properties, there are various models to study the influence of porosity on the effective mechanical properties.
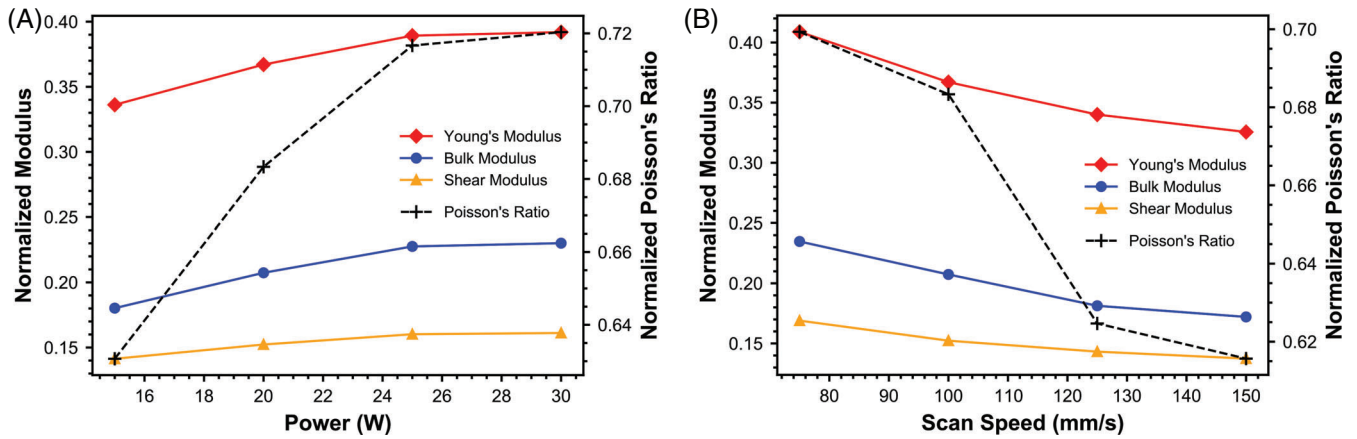
FIGURE 4   Normalized effective properties of the RVE for different process parameters. The modulus and Poisson's ratio are normalized with the bulk values E_{ss} and ν_{ss}, respectively. (A) The increase of Young's modulus and Poisson's ratio along with beam power increase. (B) The drop of Young's modulus and Poisson's ratio along with scan speed increase
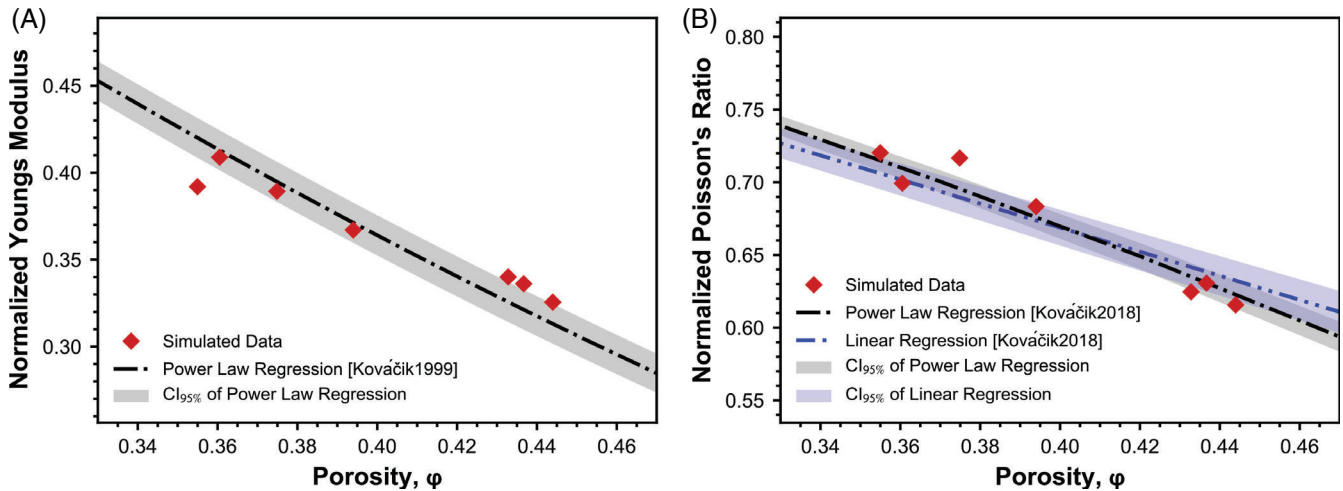

FIGURE 5   Dependence of the effective properties of the RVE on porosity. (A) For Young's modulus, the dash-dotted line is the power law model defined in Equation (23) with $f_E = 1.978 \pm 0.062$ with $R^2 = 77.0\%$. (B) For Poisson's ratio, dash-dotted line for power law model defined in Equation (25) with $f_\nu = 0.155 \pm 0.004$ and $R^2 = 93.5\%$, dashed line for linear model defined in Equation (24) with $b = -0.248 \pm 0.009$ and $R^2 = 86.5\%$

For the dependence of Young's modulus on porosity, one of the widely used models is the power law model [24]

$$E = E_{ss}(1 - \varphi)^{f_E}, \tag{23}$$

where E_{ss} is the Young's modulus of the bulk material, φ is the porosity, and f_E is the characteristic exponent for the power law dependence of the Young's modulus. This model was verified for aluminum foams by Kováčik, Marsavina, Linul [24]. Using the above equation, the dependence of Young's modulus on porosity can be established from the simulation results. Figure 5A shows the fitting results which leads to the characteristic exponent of $f_E = 1.978 \pm 0.062$ with correlation coefficient $R^2 = 77.0\%$ (note the margin of error (MoE) with 95% confidential level is employed to represent the uncertainties of regressed parameters hereinafter). This agrees well with metal foam material which is expected to be in the range of 1.8–2.2.

The dependence of Poisson's ratio on porosity is relatively less studied, and it remains an open issue [12]. There are two models which are generally used in establishing a direct relationship between Poisson's ratio and the porosity, namely a linear model and a power law model [24]

$$v = v_{ss} + b\varphi = v_{ss} + \frac{3\left(1 - 5v_{ss}\right)\left(1 - v_{ss}^2\right)}{2\left(7 - 5v_{ss}\right)}\varphi, \tag{24}$$

$$v = (v_{ss} + 1)(1 - \varphi)^{f_v} - 1, \tag{25}$$

where v_{ss} is the Poisson's ratio of the bulk material, φ is the porosity and b is a material dependent constant. It is characteristic for a particular material and is only dependent on v_0. f_v is the characteristic exponent for Poisson's ratio dependence on porosity in the power law model. The linear model does not necessarily dictate the relationship between the porosity and the resulting Poisson's ratio, and it fails at a high porosity. But for the current simulation with porosity around 0.35, both models work well as shown in Figure 5B. The simulation data of Poisson's ratio and the respective porosity were successfully regressed to the power law as well as the linear model. The fitting results of the linear model lead to the material dependent constant $b = -0.248 \pm 0.009$ with $R^2 = 86.5\%$, the fitting results of the power law model lead to characteristic exponent $f_v = 0.155 \pm 0.004$ with $R^2 = 93.5\%$. For the linear model, a large deviation of the fitting results $b = -0.248$ was found compare to analytical estimation $b = -0.124$, as well as a smaller R^2 than the power law model. Therefore, the power law model is more suitable for establishing the relationship between Poisson's ratio and porosity than the linear model.

4.3 | Residual stress

During SS the temperature field is heterogeneous and depends strongly on the powder morphology, microstructure evolution and processing parameters. The substance cools down also differently. Along with the heterogeneity of the microstructure, it gives rise to thermal residual stress. In particular, residual stress can be generated due to the thermal contraction of the new layer against the previous layers. The dependence of the thermal residual stress in the simulated microstructure upon process parameters and porosity is investigated in this subsection.

We consider the fused microstructure and let it cool down to the room temperature from the temperature profile at the last step of the phase-field simulation, as illustrated in Figures 6. The free deposited powders of the top layer can expand freely in the powder or melt state. But starting from the fused state in the last step of phase-field simulation, it is not anymore free but constrained by the surrounding material. We assume the fused top layer is stress-free at high temperature state before cooling. The thermal stress is activated when cooling starts. In the calculation of the residual stress due to thermal contraction, the constrain is enforced by applying rigid supports on the boundaries of the microstructure except for the top surface, which is set to be free. Then residual stress is evaluated as the average von Mises stress in the microstructure.

With increasing beam power, a higher temperature can be observed on the top layer of the microstructure. It leads to larger temperature gradient between the top layer and the substance, as well as a larger thermal contraction in the microstructure when cooling down to the room temperature. Therefore, at a constant scan speed of 100 mm/s, the residual stress increases with increasing beam power, as shown in Figure 6A. A larger residual stress is also found with a smaller scan speed, as shown in Figure 6B, where the beam power is 20 W for all simulations. At a lower scan speed, higher level of partial melting can be observed which results in a smaller porosity or a larger density of the microstructure. It means that the residual stress is directly dependent on the density of the microstructure manufactured in SS process. Figure 6 also shows that the stress concentration happens at the necking region of two particles where partial melting takes place.

It should be noted that the local high thermal stress can activate the plastification of the material, which goes beyond the scope of this paper. The plastic strain would turn to compensate the thermal strain, and thus it should reduce the thermal stress in the microstructure. In other words, the simulated thermal stress using linear elasticity may overestimate the residual stress in the printed part. The simulation of plastic deformation of the microstructure will be carried out in the future work.
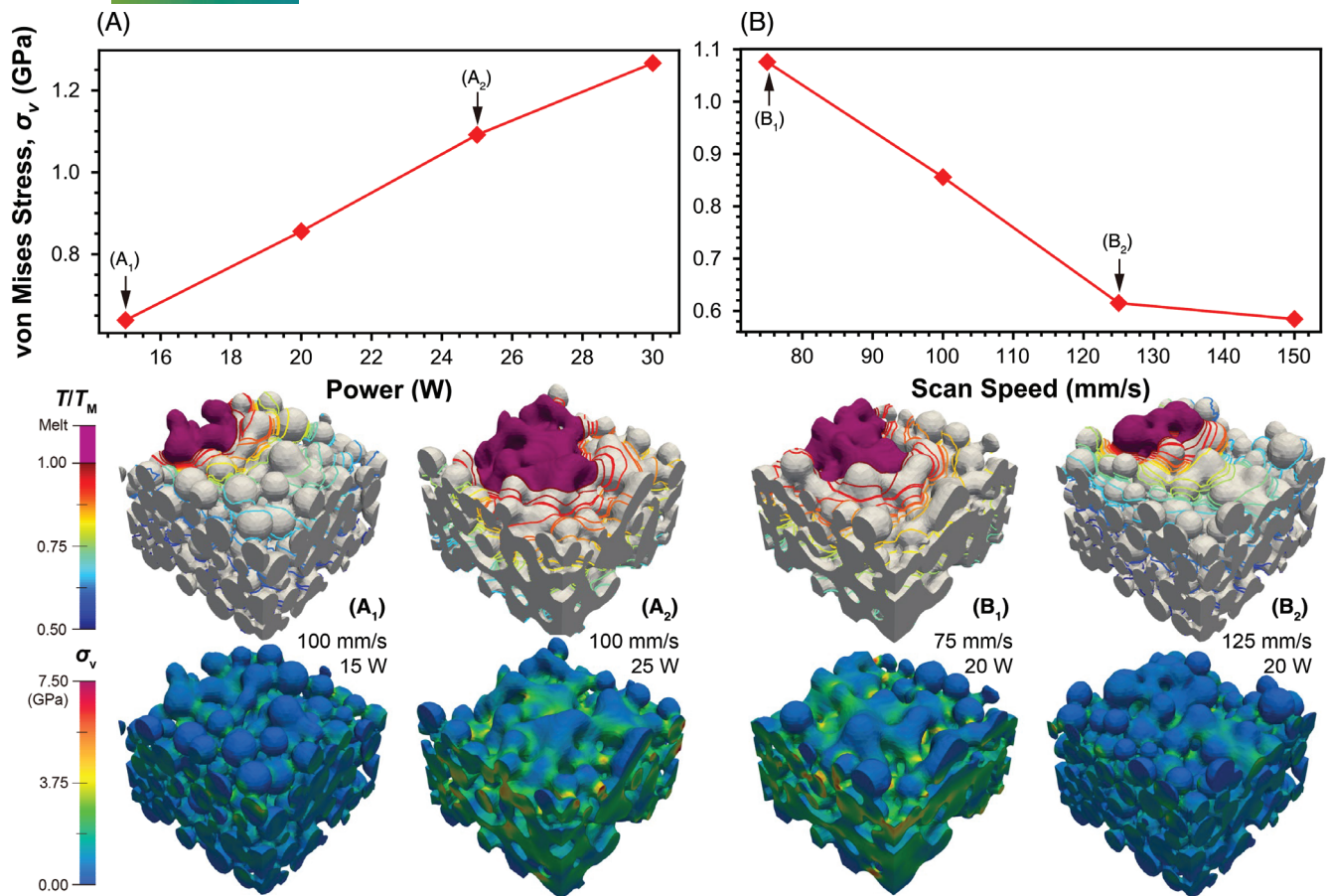
FIGURE 6 Residual stress in the RVE after cooling down from the stress free temperature to room temperature. Larger residual stress can be found with a high degree of partial melting at high beam power or small scan speed. (A) Dependence of residual stress on beam power. Profiles of the in-processing local temperature and the residual stress after cooling down to 294 K under selected beam powers (15 and 25 W) are correspondingly plotted in (A₁) and (A₂). (B) Dependence of residual stress on scan speed. Profiles of the in-processing local temperature and the residual stress after cooling down to 294 K under selected scan speeds (75 and 125 mm/s) are correspondingly plotted in (B₁) and (B₂)

5 | CONCLUSIONS

In this work, 3D multilayer phase-field simulations of the SS process and the mechanical analysis of the porous microstructure using the finite element method are presented. Different process parameters, such as beam power and scan speed, are considered to generate different microstructure. A high level of partial melting of powders is observed for a large beam power and a small scan speed, which results in small porosity of the microstructure. Furthermore, the computational homogenization analysis and mechanical analysis are performed using these microstructures to study the dependency of effective mechanical properties and residual stress on process parameters and porosity. When the beam power increases from 15 to 30 W at the same scan speed of 100 mm/s, the effective Young's modulus and the Poisson's ratio increase around 5.5% and 9.0% (normalized w.r.t. the bulk values), respectively. When the scan speed increases from 75 to 150 mm/s, the effective Young's modulus and the Poisson's ratio decrease around 8.0% and 8.5% (normalized w.r.t. the bulk values), respectively. A nonlinear relationship between the effective mechanical properties and process parameters is found. The increasing rate of effective mechanical properties decreases with increasing beam power, while increases with decreasing scan speed. The dependencies of effective Young's modulus and Poisson's ratio on porosity are well established using power law models. Stress concentrations are found at the necking region of powders, and the residual stress in the microstructure increases with increasing beam power and diminishes with increasing scan speed.

ACKNOWLEDGEMENTS

CONFLICT OF INTEREST

The authors declare no potential conflict of interests.

DATA AVAILABILITY

The authors declare that the data supporting the findings of this study are available within the paper. Source codes of MOOSE-based application NIsoS and related utilities are cured in the online repository bitbucket.org/mfm_tuda/nisos.git.

REFERENCES

[1] P. Bajaj, A. Hariharan, A. Kini, P. Kürnsteiner, D. Raabe, and E. A. Jägle, Steels in additive manufacturing: A review of their microstructure and properties, Mater. Sci. Eng. A **772** (2020), 138633.

[2] M. Beneš, V. Chalupeckỳ, and K. Mikula, Geometrical image segmentation by the Allen–Cahn equation, Appl. Numer. Math. **51** (2004), 187–205.

[3] J. Blakely and H. Mykura, Studies of vacuum annealed iron surfaces, Acta Metall. **11** (1963), 399–404.

[4] M. Carraturo, J. Jomo, S. Kollmannsberger, A. Reali, F. Auricchio, and E. Rank, Modeling and experimental validation of an immersed thermo-mechanical part-scale analysis for laser powder bed fusion processes, Addit Manuf **36** (2020), 101498.

[5] M. W. Chase Jr., Nist-janaf thermochemical tables, J. Phys. Chem. Ref. Data Monograph **9** (1998), 7.

[6] M. Chiumenti, E. Neiva, E. Salsi, M. Cervera, S. Badia, J. Moya, Z. Chen, C. Lee, and C. Davies, Numerical modelling and experimental validation in selective laser melting, Addit. Manuf. **18** (2017), 171–185.

[7] R. Chojowski, U. S. Schwarz, and F. Ziebert, Reversible elastic phase field approach and application to cell monolayers, Eur. Phys. J. E **43** (2020), 1–12.

[8] A. Di Schino, J. Kenny, and G. Abbruzzese, Analysis of the recrystallization and grain growth processes in aisi 316 stainless steel, J. Mater. Sci. **37** (2002), 5291–5298.

[9] C. M. Elliott, D. A. French, and F. Milner, A second order splitting method for the Cahn-Hilliard equation, Numer. Math. **54** (1989), 575–590.

[10] S. Eshraghi and S. Das, Mechanical and microstructural properties of polycaprolactone scaffolds with one-dimensional, two-dimensional, and three-dimensional orthogonally oriented porous architectures produced by selective laser sintering, Acta Biomater. **6** (2010), 2467–2476.

[11] R. Ganeriwala, M. Strantza, W. King, B. Clausen, T. Q. Phan, L. E. Levine, D. W. Brown, and N. Hodge, Evaluation of a thermomechanical model for prediction of residual stress during laser powder bed fusion of ti-6al-4v, Addit. Manuf. **27** (2019), 489–502.

[12] E. Gregorová, W. Pabst, T. Uhlířová, V. Nečina, M. Veselỳ, and I. Sedlářová, Processing, microstructure and elastic properties of mullite-based ceramic foams prepared by direct foaming with wheat flour, J. Eur. Ceramic Soc. **36** (2016), 109–120.

[13] D. Gu, W. Meiners, K. Wissenbach, and R. Poprawe, Laser additive manufacturing of metallic components: Materials, processes and mechanisms, Int. Mater. Rev. **57** (2012), 133–164.

[14] A. Gusarov, I. Yadroitsev, P. Bertrand, and I. Smurov, Model of radiation and heat transfer in laser-powder interaction zone at selective laser melting, J. Heat Transf. **131** (2009), 072101.

[15] T. Hoshino, K. Mito, A. Nagashima, and M. Miyata, Determination of the thermal conductivity of argon and nitrogen over a wide temperature range through data evaluation and shock-tube experiments, Int. J. Thermophys. **7** (1986), 647–662.

[16] A. Hussein, L. Hao, C. Yan, and R. Everson, Finite element simulation of the temperature and stress fields in single layers built without-support in selective laser melting, Mater. Des. **52** (2013), no. 1980-2015, 638–647.

[17] K. J. Jhong and W. H. Lee, Fabricating soft maganetic composite by using selective laser sintering, Proc. 2016 IEEE Int Conf. Ind. Technol. (ICIT), 2016, pp. 1115–1118.

[18] W. Jiang, Y. Luo, B. Wang, W. Woo, and S. T. Tu, Neutron diffraction measurement and numerical simulation to study the effect of repair depth on residual stress in 316L stainless steel repair weld, ASME. J. Pressure Vessel Technol. **137** (2015), 041406.

[19] K. John, P. Peyla, K. Kassner, J. Prost, and C. Misbah, Nonlinear study of symmetry breaking in Actin gels: Implications for cellular motility, Phys. Rev. Lett. **100** (2008), 068101.

[20] D. A. Kay and A. Tomasi, Color image segmentation by the vector-valued Allen–Cahn phase-field model: A multigrid solution, IEEE Trans. Image Process. **18** (2009), 2330–2339.

[21] S. A. Khairallah, A. A. Martin, J. R. Lee, G. Guss, N. P. Calta, J. A. Hammons, M. H. Nielsen, K. Chaput, E. Schwalbach, M. N. Shah, et al., Controlling interdependent meso-nanosecond dynamics and defect generation in metal 3D printing, Science **368** (2020), 660–665.

[22] S. H. Ko, H. Pan, C. P. Grigoropoulos, C. K. Luscombe, J. M. Fréchet, and D. Poulikakos, All-inkjet-printed flexible electronics fabrication on a polymer substrate by low-temperature high-resolution selective laser sintering of metal nanoparticles, Nanotechnology **18** (2007), 345202.

[23] C. Körner, M. Markl, and J. A. Koepf, Modeling and simulation of microstructure evolution for additive manufacturing of metals: A critical review, Metall. Mater. Trans. A **51** (2020), 4970–4983.

[24] J. Kováčik, L. Marsavina, and E. Linul, Poisson's ratio of closed-cell aluminium foams, Materials **11** (2018), 1904.

[25] S. Kumar, Selective laser sintering: A qualitative and objective approach, JOM **55** (2003), 43–47.

[26] P. Leo, J. Lowengrub, and H. J. Jou, A diffuse interface model for microstructural evolution in elastically stressed solids, Acta Mater. **46** (1998), 2113–2130.

[27] J. Q. Li, T. H. Fan, T. Taniguchi, and B. Zhang, Phase-field modeling on laser melting of a metallic powder, Int. J. Heat Mass Transf. **117** (2018), 412–424.

[28] F. Liu, Q. Zhang, W. Zhou, J. Zhao, and J. Chen, Micro scale 3D FEM simulation on thermal evolution within the porous structure in selective laser sintering, J. Mater. Process. Technol **212** (2012), 2058–2065.

[29] Z. Luo and Y. Zhao, A survey of finite element analysis of temperature and thermal stress fields in powder bed fusion additive manufacturing, Addit. Manuf. **21** (2018), 318–332.

[30] M. Markl and C. Körner, Multiscale modeling of powder bed–based additive manufacturing, Ann. Rev. Mater. Res. **46** (2016), 93–123.

[31] H. Mead and C. Birchenall, Self-diffusion of iron in austenite, JOM **8** (1956), 1336–1339.

[32] N. Moelans, B. Blanpain, and P. Wollants, Quantitative analysis of grain boundary properties in a generalized phase field model for grain growth in anisotropic systems, Phys. Rev. B **78** (2008), 024113.

[33] G. Moraitis and G. Labeas, Residual stress and distortion calculation of laser beam welding for aluminum lap joints, J. Mater. Process. Technol. **198** (2008), 260–269.

[34] E. National Academies of Sciences, Medicine, *Frontiers of materials research: A decadal survey*, Washington DC: National Academies Press, 2019.

[35] M. Nicoli, M. Plapp, and H. Henry, Tensorial mobilities for accurate solution of transport problems in models with diffuse interfaces, Phys. Rev. E **84** (2011), 046707.

[36] E. O. Olakanmi, R. Cochrane, and K. Dalgarno, A review on selective laser sintering/melting (SLS/SLM) of aluminium alloy powders: Processing, microstructure, and properties, Prog. Mater. Sci. **74** (2015), 401–477.

[37] C. Panwisawas, Y. T. Tang, and R. C. Reed, Metal 3D printing as a disruptive technology for superalloys, Nat. Commun. **11** (2020), 1–4.

[38] L. Parry, I. Ashcroft, and R. D. Wildman, Understanding the effect of laser scan strategy on residual stress in selective laser melting through thermo-mechanical simulation, Addit. Manuf. **12** (2016), 1–15.

[39] K. Prashanth, S. Scudino, T. Maity, J. Das, and J. Eckert, Is the energy density a reliable parameter for materials synthesis by selective laser melting? Mater. Res. Lett. **5** (2017), 386–390.

[40] K. Ren, Y. Chew, J. Fuh, Y. Zhang, and G. Bi, Thermo-mechanical analyses for optimized path planning in laser aided additive manufacturing processes, Mater. Des **162** (2019), 80–93.

[41] J. Schröder (2014) *A numerical two-scale homogenization scheme: the FE2-method*. In: J. Schröder, K. Hackl (eds) *Plasticity and Beyond*. CISM International Centre for Mechanical Sciences, vol 550. Springer, Vienna.

[42] S. L. Sing, W. Y. Yeong, F. E. Wiria, B. Y. Tay, Z. Zhao, L. Zhao, Z. Tian, and S. Yang, Direct selective laser sintering and melting of ceramics: A review, Rapid Prototyp. J. **23** (2017), 611–623.

[43] V. Smil, *Making the modern world: Materials and dematerialization*, 1st ed., Wiley, Weinheim, 2013.

[44] I. Steinbach, Phase-field model for microstructure evolution at the mesoscopic scale, Ann. Rev. Mater. Res. **43** (2013), 89–107.

[45] K. Tan, C. Chua, K. Leong, C. Cheah, W. Gui, W. Tan, and F. Wiria, Selective laser sintering of biocompatible polymers for applications in tissue engineering, Bio-Med. Mater. Eng. **15** (2005), 113–124.

[46] I. Temizer, *Homogenization in linear and non-linear elasticity*, University of California, Berkeley, 2005.

[47] M. R. Tonks, D. Gaston, P. C. Millett, D. Andrs, and P. Talbot, An object-oriented finite element framework for multiphysics phase field simulations, Comput. Mater. Sci. **51** (2012), 20–29.

[48] G. Vastola, G. Zhang, Q. Pei, and Y. W. Zhang, Controlling of residual stress in additive manufacturing of ti6al4v by finite element modeling, Addit. Manuf. **12** (2016), 231–239.

[49] Y. U. Wang, Computer modeling and simulation of solid-state sintering: A phase field approach, Acta Mater. **54** (2006), 953–961.

[50] J. M. Williams, A. Adewunmi, R. M. Schek, C. L. Flanagan, P. H. Krebsbach, S. E. Feinberg, S. J. Hollister, and S. Das, Bone tissue engineering using polycaprolactone scaffolds fabricated via selective laser sintering, Biomaterials **26** (2005), 4817–4827.

[51] R. J. Williams, C. M. Davies, and P. A. Hooper, A pragmatic part scale model for residual stress and distortion prediction in powder bed fusion, Addit Manuf **22** (2018), 416–425.

[52] F. Xie, X. He, S. Cao, and X. Qu, Structural and mechanical characteristics of porous 316l stainless steel fabricated by indirect selective laser sintering, J. Mater. Process. Technol. **213** (2013), 838–843.

[53] Y. Yang, P. Kühn, M. Yi, H. Egger, and B. X. Xu, Non-isothermal phase-field modeling of heat–melt–microstructure-coupled processes during powder bed fusion, JOM **72** (2020), 1719–1733.

[54] Y. Yang, T. D. Oyedeji, P. Kühn, and B. X. Xu, Investigation on temperature-gradient-driven effects in unconventional sintering via non-isothermal phase-field simulation, Scr. Mater. **186** (2020), 152–157.

[55] Y. Yang, O. Ragnvaldsen, Y. Bai, M. Yi, and B. X. Xu, 3D non-isothermal phase-field simulation of microstructure evolution during selective laser sintering, Npj Comput. Mater. **5** (2019), 81.

[56] M. Yi, B. X. Xu, and O. Gutfleisch, Computational study on microstructure evolution and magnetic property of laser additively manufactured magnetic materials, Comput. Mech. **64** (2019), 917–935.

[57] M. A. Zaeem and H. El Kadiri, An elastic phase field model for thermal oxidation of metals: Application to zirconia, Comput. Mater. Sci. **89** (2014), 122–129.

[58] Y. Zhao, P. Stein, and B. X. Xu, Isogeometric analysis of mechanically coupled Cahn–Hilliard phase segregation in hyperelastic electrodes of Li-ion batteries, Comput. Methods Appl. Mech. Eng. **297** (2015), 325–347.

[59] O. Zinovieva, A. Zinoviev, and V. Ploshikhin, Three-dimensional modeling of the microstructure evolution during metal additive manufacturing, Comput. Mater. Sci. **141** (2018), 207–220.